Wide-Angle Sparse 3D Synthetic Aperture Radar Imaging for Nonlinear Flight Paths

Christian D. Austin and Randolph L. Moses
The Ohio State University, Department of Electrical and Computer Engineering
2015 Neil Avenue, Columbus, OH 43210, USA
Email: {austinc, randy}@ece.osu.edu

***Abstract*—Conventional three-dimensional (3D) Fourier synthetic aperture radar (SAR) imaging requires a collection of radar returns from multiple linear passes over a scene. Image resolution is improved by increasing the extent of these passes in azimuth and elevation. Hence, high resolution imagery requires large data collection times and storage capacity. In this work we investigate wide-angle 3D SAR image reconstruction for a sparse nonlinear collection path. This collection modality requires less data acquisition time and storage capacity than conventional linear collection. Images are reconstructed from measured radar returns using ℓ_1-penalized least-squares inversion. An example is presented demonstrating that images with well-resolved features can be formed using data collected along a sparse nonlinear path.**

I. Introduction

Synthetic aperture radar (SAR) is an all-weather, persistent, and large standoff distance imaging technique. SAR images are pixels or voxels representing the complex valued electromagnetic reflectivity of the scene. When scene size is small or the standoff distance from the radar to scene center is large, electromagnetic wavefront curvature is negligible. For a transmitted FM chirp signal and negligible wavefront curvature, the collected electromagnetic return can be interpreted as a portion of a radial line from the radar to scene center in 3D k-space (spatial frequency domain) of the image [1]; thus, the radar flight path determines which portion of the scene's k-space is collected. In general, scene reflectivity, and hence k-space data, is a function of signal polarization and the azimuth and elevation angle that the radar illuminates the scene from.

Currently, 2D linear flight path SAR imaging is prevalent. A linear flight path is approximately a straight line path with a constant standoff distance from scene center; the aperture of k-space data collected over a linear flight path is approximately planar. 3D imaging is desirable for applications such as automatic target recognition or topographic mapping. Using conventional Fourier inversion imaging techniques, 3D SAR images that are well-resolved in all dimensions require closely spaced samples from many linear flight passes over a scene [2]; large data storage and collection time is needed for this type of imaging.

To decrease storage and time requirements, a subset of the k-space data needed to form well-resolved images can be collected. Conventional Fourier inversion image formation can be used on this subset of data, but the reconstructed image will be smoothed and contain artifacts. Smoothing and artifacts can be explained by the point spread function (PSF) of the image, defined by the Fourier transform of the data subset indicator function. The mainlobe of this PSF will typically be wider and the sidelobes higher than for the PSF of an image formed from the full set of k-space data (see e.g. [3]).

Many algorithms exist for reconstructing SAR images from a sparse subset of k-space data without incurring the smoothing and artifacts present in a standard Fourier image. Improvement in imaging performance is typically gained by imposing model or data collection assumptions. Interferometric synthetic aperture radar (IFSAR) processing is one such sparse 3D image reconstruction algorithm. This imaging method uses two 2D images formed from two linear flight paths closely spaced in elevation angle with the same azimuth extent and assumes scattering centers are well-resolved. The third, height dimension is calculated as the pairwise phase difference between pixels in each image [1], [4]. Another algorithm, CLEAN, can be used for 3D image reconstruction using sparse k-space data collected from an arbitrary flight path. This is an iterative greedy algorithm that assumes a point scattering center model and adds point scatterers to the model at each iteration [3], [5].

Typically, scenes are sparse, meaning that there are only a small number of prominent scattering centers. Under scattering center sparsity assumptions, convex optimization can be used for SAR image reconstruction [6]. This method of image reconstruction fits a point scatterer model to the measured k-space data under an ℓ_l penalty. Sparse reconstruction has been shown to produce well-resolved, 2D SAR image reconstructions using sparse sets of k-space data [6]–[8].

In this work, we investigate 3D wide-angle sparse image reconstruction using k-space data collected from multiple polarizations on a nonlinear flight path. A nonlinear path is used to collect a diverse subset of k-space data from the set of data used in conventional linear flight path imaging, and sparse reconstruction is used to reconstruct an image consistent with the collected k-space data. The objective of the imaging algorithm is to produce accurate well-resolved 3D images without incurring the time and storage costs required in conventional linear path imaging. In Section II, we describe SAR

This work was performed under Ohio Space Grant Consortium fellowship funding.

data collection and present a SAR scattering center model; Section III discusses an algorithm for 3D wide-angle multiple polarization image reconstruction for an arbitrary flight path. Finally, in Section IV, we present a 3D image reconstruction example using an Air Force Research Lab (AFRL) challenge problem dataset. This dataset consists of k-space data from three polarizations collected on a nonlinear continuous pseudo-random path [9]. This example demonstrates that it is possible to form accurate 3D SAR images with well-resolved features from data collected along a nonlinear flight path.

II. SAR Data Collection and Model

In the remainder of this document, it is assumed that wavefront curvature is negligible and that the radar transmits an FM chirp signal,

$$e^{j\left(\omega_c t+\alpha t^2\right)}, \tag{1}$$

where α is the chirp rate, and ω_c is the center frequency of the radar. The bandwidth of this signal, $BW = 2\alpha\tau_c$, is given by the product of the chirp rate and the chirp duration τ_c. After mixing the return signal with the transmitted signal, delayed by the time to scene center, demodulating, and neglecting a quadratic phase term, the final received signal is [1]

$$r(t) = \int_{-B_z}^{B_z}\int_{-B_y}^{B_y}\int_{-B_x}^{B_x} a(x,y,z,\theta_{\text{az}},\theta_{\text{el}},f,pol) \times e^{-jX(t)x}\mathrm{d}x\mathrm{d}y\mathrm{d}z. \tag{2}$$

The coordinate x is defined as the radial line from the radar to scene center, and y, and z are orthogonal to x and each other. This coordinate system changes over the radar's flight path. The scene reflectivity function is given by $a(x,y,z,\theta_{\text{az}},\theta_{\text{el}},f,pol)$. Angles θ_{az} and θ_{el} are the azimuth and elevation angles of the radar with respect to a fixed ground plane coordinate system; f is the frequency of the radar signal, and pol is the polarization of the radar signal. Boundaries of the scene in each dimension are $B_{(\cdot)}$. The function $X(t)$ is a linear function of time and is supported on $[\frac{2}{c}(\omega_c - \pi BW),\ \frac{2}{c}(\omega_c + \pi BW)]$ rad/m, where c is the speed of light in m/s, and BW is the chirp bandwidth in Hz.

Since $e^{-jX(t)x}$ is the Fourier kernel, (2) is the Fourier transform of the scene reflectivity function projected onto the x dimension. By the projection-slice theorem [1], it follows that Fourier transform of the scene reflectivity function projection onto the x dimension is equivalent to a line along the x-axis in 3D k-space of the scene reflectivity function. The frequency support of each line is that of $X(t)$; so, each line has a bandwidth of $\frac{4\pi BW}{c}$ rad/m centered at $\frac{2\omega_c}{c}$ rad/m. The flight path defines which lines in k-space are collected, and hence what subset of k-space is sampled.

We model a SAR scene as collection of polarization-dependent anisotropic scattering centers. The scene reflectivity function of this model is the image that we wish to recover and is ideally represented as a summation of N_s complex weighted impulses at the location of each point scattering center. In k-space, the scattering center model is

$$F(X,Y,Z) = \sum_{k=1}^{N_s} a_k(\theta_{\text{az}},\theta_{\text{el}},f,pol)e^{-j(Xx_k+Yy_k+Zz_k)}. \tag{3}$$

Variables x_k, y_k, and z_k are the (x,y,z) spatial coordinates of scattering center k in units of meters, and X, Y, and Z are the spatial frequency coordinates of 3D k-space in units of rad/m . The complex amplitude of scattering center k, a_k, is a function of the radar azimuth angle, θ_{az}, elevation angle, θ_{el}, frequency, f, and polarization, pol.

III. Image Reconstruction

In this section, we discuss an algorithm for wide-angle multiple polarization 3D SAR image reconstruction from noncoherent combinations of images formed using sparse reconstruction on subsets of k-space data. This algorithm assumes the scattering center model (3), that the complex magnitude response of each scattering center is approximately constant over narrow aspect angles and across the radar frequency bandwidth, and that the image is sparse; there are no requirements on the type of flight path or amount of data collected, although these factors will affect reconstructed image accuracy.

A. Sparse ℓ_1-norm reconstruction

Scattering center locations are unknown; a set of N locations are chosen as candidate scattering center locations,

$$C = \{(x_k,y_k,z_k)\}_{k=1}^{N}. \tag{4}$$

Define an $M \times N$ measurement matrix by

$$A = \left[e^{-j(X_m x_k+Y_m y_k+Z_m z_k)}\right],$$

where m indexes M measured k-space frequencies down rows, and k indexes the N coordinates in C across columns. Under the assumption that scattering center amplitude is constant over narrow aspect angle extent and throughout the radar bandwidth, the measured data from the scattering center model, (3), can be written in matrix form as

$$y = Ax + n, \tag{5}$$

where x is the N-dimensional vectorized image that we wish to reconstruct; it has complex amplitude value a_k in row k if a scattering center is located at (x_k,y_k,z_k) and zero otherwise; the image vector x maps to the 3D image, $I(x_k,y_k,z_k)$, by the relation $I(x_k,y_k,z_k) = x(i)$ if and only if column i of A is from coordinate (x_k,y_k,z_k). The vector n is an M dimensional i.i.d. circular complex Gaussian noise vector with zero mean and variance σ_n^2, and y is an M-dimensional vector of noisy k-space measurements.

The number of scattering centers is assumed to be sparse with respect to the number of image voxels in x. A reconstructed image, $\hat{x}$, is the solution to the sparse optimization problem [6], [7]

$$\hat{x} = \underset{x}{\text{argmin}}\ \|y - Ax\|_2^2 + \lambda\|x\|_1, \tag{6}$$

referred to as basis pursuit denoising (BPDN) in some literature [10], [11]. The p-norm is denoted as $\|\cdot\|_p$, and λ is a sparsity penalty parameter. Define uniform partitions on the x, y, and z spatial axes with partition spacings of Δx,Δy, and Δz, respectively. Let the set of candidate coordinates C in (4) consist of all permutations of (x, y, z) coordinates from the partitioned axes; then, the set C defines a uniform 3D grid on the scene. If, in addition, the k-space samples are on a uniform 3D frequency grid, the operation Ax can be implemented using the computationally efficient 3D Fast Fourier Transform (FFT) operation. Defining the set C is an algorithmic choice, and can be chosen as a uniform 3D grid. However, k-space data is offset from the origin, and samples do not lie on a 3D uniform grid. To use the 3D FFT, this data must be shifted to the origin of k-space and interpolated to a uniform grid, as discussed next.

B. K-space Processing

Collected k-space data is contained in a bounding box with bandwidths of $(X_{\text{BW}}, Y_{\text{BW}}, Z_{\text{BW}})$ in the X, Y, and Z dimensions. Define the center coordinate of the bounding box as (X_c, Y_c, Z_c). Shifting the center of the bounding box to the origin centers k-space data at the origin. The Fourier Transform of the original data is equal to the Fourier transform of the shifted data multiplied by the phase ramp $e^{j(X_c x + Y_c y + Z_c z)}$; so, the Fourier transform can be applied to the k-space data as if it were centered at the origin, if the transform is multiplied by the appropriate phase ramp.

There are many algorithms for data interpolation. Two methods of k-space data interpolation to a uniform 3D grid are explored here and applied to the example in Section IV. The first method is a simple nearest-neighbor (NN) method. In this method, the k-space bounding box is divided into a uniform grid. For each grid point, if there is k-space data within a box centered about the grid point with edges of length ΔX,ΔY, and ΔZ, the grid point is set to the value of the data point nearest in Euclidean distance to the grid point; otherwise, the grid point is set to zero. The second method uses kernel smoothing [12]. As in NN interpolation, if there are no k-space data points within a box centered at a grid point with edges of length ΔX,ΔY, and ΔZ, then the grid point is set to zero; otherwise, a kernel weighting function is used to interpolate the grid point with local data.

C. Noncoherent Image Combination

Scattering centers in model (3) are anisotropic and polarization dependent; so, their complex amplitude changes over wide azimuth and elevation angles and for different polarizations. The scattering center model, (5), used in image reconstruction assumes that data is collected over narrow aspect angles so that the complex amplitude is approximately constant. Since the k-space data may extend over wide angles, we divide the complete dataset into narrow angle subsets and reconstruct an image using each subset. A common size bounding box is used for all subsets. The common size ensures that voxels in each reconstructed image will be at the same locations.

Different scattering centers will appear in images formed from different k-space subsets and polarization data since scattering centers may only persist over limited aspect angles, and only have non-negligible response at certain polarizations. We combine all images into one wide-angle, multiple polarization image containing information about all scattering scattering centers. In [13], [14], SAR azimuth subset images are combined noncoherently using a GLRT approach. We apply a similar image formation method, incorporating all subset images from all polarizations. The final noncoherent image is defined as

$$I(x_k, y_k, z_k) = \max_{\theta_{\text{az}_c}, \theta_{\text{el}_c}, pol} \left| I(x_k, y_k, z_k; \theta_{\text{az}_c} \theta_{\text{el}_c}, pol) \right| . \quad (7)$$

Coordinates x_k, y_k, and z_k are locations of reconstructed image voxels, and $I(x_k, y_k, z_k; \theta_{\text{az}_c}, \theta_{\text{el}_c}, pol)$ denotes a subset image formed using data centered at azimuth and elevation angles θ_{az_c}, θ_{el_c} and from polarization pol. We note that the final image is a real-valued image of voxel magnitude. Image reconstruction steps are summarized in Algorithm 1.

Algorithm 1 Image Reconstruction

1) For each polarization, partition k-space data into subsets over a narrow range of azimuth and elevation angles.
2) Define a common bounding box large enough to cover each individual subset of data. One possibility is to define bounding boxes for each data subset and take the maximum box width in each dimension to be the common bounding box width in each respective dimension.
3) Shift each subset of data to the origin of k-space and interpolate the data to a uniform grid within the bounding box.
4) Reconstruct images from each shifted and interpolated subset of k-space data by solving the sparse optimization problem (6).
5) Form one noncoherent image by combining all subset images using (7).

The preceding image reconstruction discussion assumed negligible wavefront curvature. It may be possible to modify the image reconstruction algorithm for non-negligible wavefront curvature by using a measurement matrix A that incorporates wavefront curvature. However, it may not be possible to represent this measurement matrix implicitly as a computationally efficient operation such as the 3D FFT used here.

IV. Image Reconstruction Example

Reconstructed 3D images using Algorithm 1 and k-space data from an AFRL challenge problem dataset [15] are presented in this section. Data is generated by the Visual-D electromagnetic scattering simulator for a radar with center frequency $f_c = 10$ GHz and bandwidth $BW = 6$ GHz and consists of k-space samples collected along a continuous pseudo-random "squiggle" path from a construction backhoe scene. Three polarizations are included in the dataset,

vertical-vertical, horizontal-horizontal, and cross-polarization. The trace in Figure 1 shows the squiggle path as a parametric plot of azimuth and elevation angle, defined with respect to a fixed ground plane coordinate system, and Figure 2 displays k-space data that can be collected by the radar, which is contained between the inner and outer domes. The squiggle path is superimposed on the outer dome. The set of k-space data collected along the squiggle path is very sparse with respect to the full data dome.

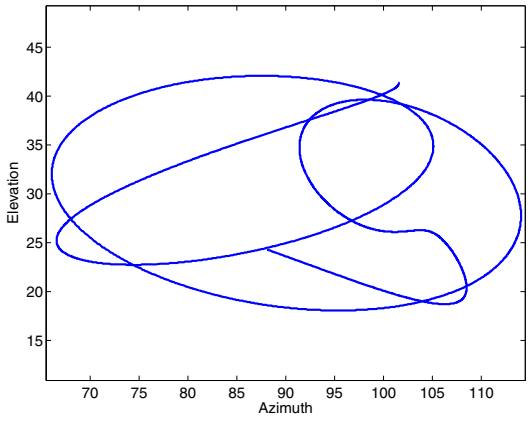

Fig. 1. Squiggle path as a function of azimuth and elevation angle in degrees.

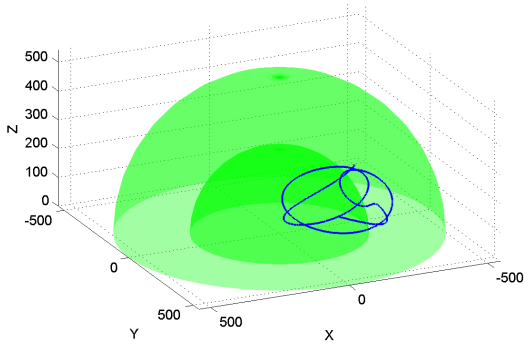

Fig. 2. Data dome of all k-space data that can be collected by a radar shown in units of rad/m. Support of the k-space data is contained between the inner and outer dome. An outline on the outer dome shows the location of "squiggle path" k-space data, which extends from the outline radially to the inner dome.

For all polarizations, the azimuth and elevation range of the squiggle path are approximately $[66°, 114.1°]$, and $[18°, 42.1°]$, respectively. Squiggle path k-space data is partitioned into overlapping subsets with azimuth angle extent of $10°$ and full elevation extent at $5°$ azimuth increments; so, subset k consists of squiggle path data from all elevation angles in the azimuth range $[66° + (k-1)5°, 66° + (k-1)5° + 10°)$ for $k = 1, \ldots, 9$. Figure 3 shows the magnitude of k-space data from the k-space subset in azimuth range of $[66°, 76°)$.

Each subset of data is contained in a bounding box with bandwidths in each dimension of $(X_{\text{BW}}, Y_{\text{BW}}, Z_{\text{BW}}) = (142.80, 314.2, 285.6)$ rad/m. At these bandwidths, spatial samples are critically sampled with sample spacings of $(\Delta x, \Delta y, \Delta z) = (0.044, 0.02, 0.022)$ meters in each respective dimension. Both the image reconstruction and k-space interpolation are performed on uniformly spaced $182 \times 250 \times 252$ grids. With this size grid, the spatial extent of the reconstructed images is $[-4, 3.97] \times [-2.5, 2.48] \times [-2.77, 2.75]$ meters in the x, y, and z dimensions respectively.

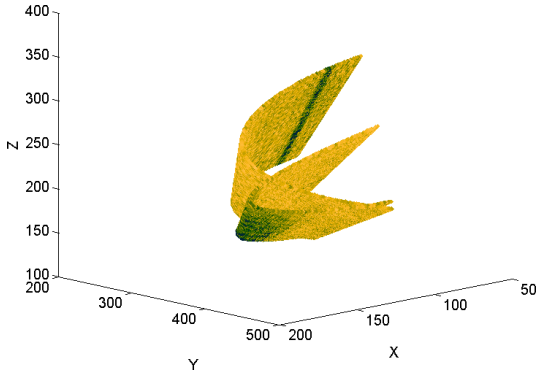

Fig. 3. Magnitude of k-space data subset from azimuth range $[66°, 76°)$. Lighter colors and smaller points are used for smaller magnitude samples; darker colors and larger points are used for larger magnitude samples. Axes units are in rad/m.

The squiggle path dataset is noiseless. Before interpolation, we corrupt all subsets of k-space data with i.i.d. circular complex Gaussian noise with zero mean and variance, $\sigma_n^2 = 0.9$. Real and imaginary parts of the k-space data have a mean of approximately zero and variance, σ_s^2, of approximately 9. Noise variance is chosen so that the signal to noise ratio (SNR) is 10 dB, where SNR in decibels is defined as $10 \log(\frac{\sigma_s^2}{\sigma_n^2})$. Each subset of k-space data is interpolated using NN interpolation. Images formed using both Epanechnikov and Gaussian kernel interpolated data appeared nearly identical to images formed using NN interpolation at the cost of a large increase in computation time.

Images are reconstructed from each subset of noisy data and all polarizations by solving the sparse optimization problem (6), producing 27 reconstructed subset images. We use a modified version of the monotonic iterative algorithm code from [7] to solve the optimization problem. The modified version operates directly on k-space data and does not require the formation or convolution with a PSF, reducing computation time and memory requirements. All images are reconstructed using a sparsity parameter $\lambda = 10$. Selection of λ is an ongoing area of research [16], [17]. Here, λ was chosen empirically through visual inspection of images. The final image is formed noncoherently by combining all subset images according to (7).

All simulations were performed in MATLAB on a system with an Intel 3 GHz Dual Core Xeon processor and 4 GB of memory. The most computationally intensive steps of image reconstruction are interpolation and sparse optimization. Nearest-neighbor interpolation took less than 25 seconds to run on each data subsets, and sparse optimization took between

17 and 26 minutes to run on each subset. Although not investigated here, it may be possible to alter stopping criterion tolerances in the monotonic iterative algorithm to lower run times without adversely affecting reconstructed images.

Figure 4 shows a side view of the benchmark 3D reconstructed backhoe image supplied with the squiggle path dataset. The image was formed using k-space data collected at every $\frac{1}{14}^\circ$ in azimuth and elevation angle along an azimuth range of $[65.5^\circ, 114.5^\circ]$ and elevation range of $[17.5^\circ, 42.5^\circ]$. Squiggle path k-space data is contained within this benchmark dataset and is very sparse with respect to it; the squiggle path data set consists of approximately 1.29% of the benchmark data samples.

(a)

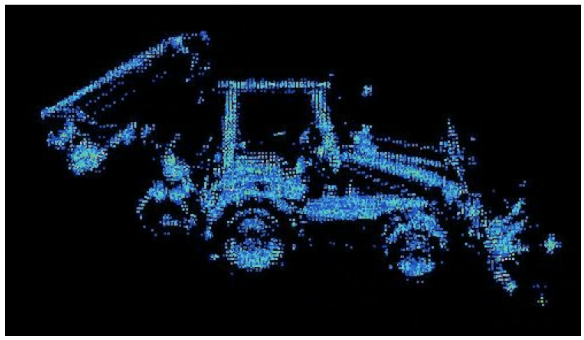

(b)

Fig. 4. Benchmark reconstructed backhoe image using k-space data collected at every $\frac{1}{14}^\circ$ in azimuth and elevation angle along an azimuth range of $[65.5^\circ, 114.5^\circ]$ and elevation range of $[17.5^\circ, 42.5^\circ]$. Subfigure (a) displays the reconstructed image superimposed on the backhoe facet model, and (b) shows the reconstructed image without the facet model.

A reconstructed squiggle path image viewed from the side and top is shown in Figure 6. The image is formed using Algorithm 1 and conventional 3D FFT image reconstruction, instead of sparse reconstruction in step 4) of the reconstruction algorithm. The top 25 dB magnitude voxels are displayed in the image. Structure of the backhoe is highly smoothed and distorted, and backhoe features, such as the front scoop are not well localized. If a larger range of voxels is displayed, it becomes difficult to visually localize any backhoe features. Poor image quality could be predicted from the PSF of the squiggle path, shown in Figure 5, which is not well localized and exhibits spreading in each dimension.

Figure 7 shows a side and top view of a reconstructed squiggle path image using Algorithm 1; the top 30 dB magnitude voxels are displayed. Features in the reconstructed image are well-resolved. For example, the hood, roof, and front and back scoops are clearly visible, in the correct location, and are not smoothed along many voxels. The side panels of the driver cab are not visible, and the arm on the back scoop is not as prominent as in the benchmark in Figure 4, but most backhoe features in the benchmark backhoe image are also visible in the squiggle path reconstruction. There are some artifacts in the image that do not lie close to the backhoe, namely below the front and back scoop; however, most voxels correspond to features on the backhoe. From the top view of the backhoe, the group of voxels at the top left also appear to be present in the benchmark image as viewed from an angle not shown here; these voxels are probably a result of multibounce off of the back scoop and are not artifacts specific to squiggle path reconstruction. It should be noted that since a smaller range of voxels are plotted in the conventional reconstruction, voxels appear on features, such as on the roof and wheels, in the sparse reconstructed image that do not appear in the conventional reconstruction.

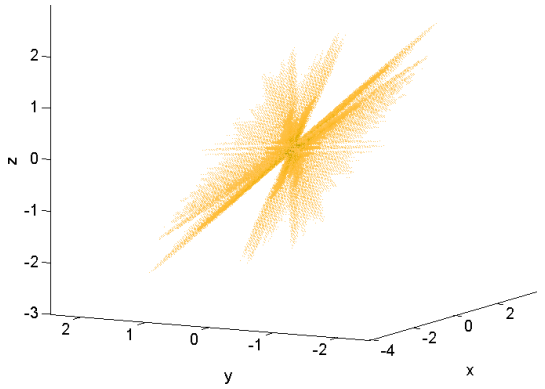

Fig. 5. Magnitude of PSF from the squiggle path over azimuth range $[66^\circ, 76^\circ)$. Light colors and small points are used for small magnitude voxels; darker colors and large points are used for large magnitude voxels. Axis units are in meters.

The reconstruction in Figure 7 is displayed as raw reconstructed image voxels, with one point representing a voxel. If the final image is for human interpretation, post-processing can be applied to the reconstructed backhoe image to improve visualization. Figure 8 shows a side and top view of the same reconstructed backhoe image as in Figure 7, but with additional visualization post-processing. The reconstructed image from step 5) of Algorithm 1 is smoothed using a Gaussian kernel with diagonal covariance and standard deviation of 2 voxels in each dimension; smoothed image voxel magnitude contours are displayed. Figure 8 displays 200 contour levels equally spaced between the minimum and maximum voxel values. Color darkens and transparency becomes more opaque as contour level increases. When using this method of visualization, local pixel groups appear as surfaces on the backhoe.

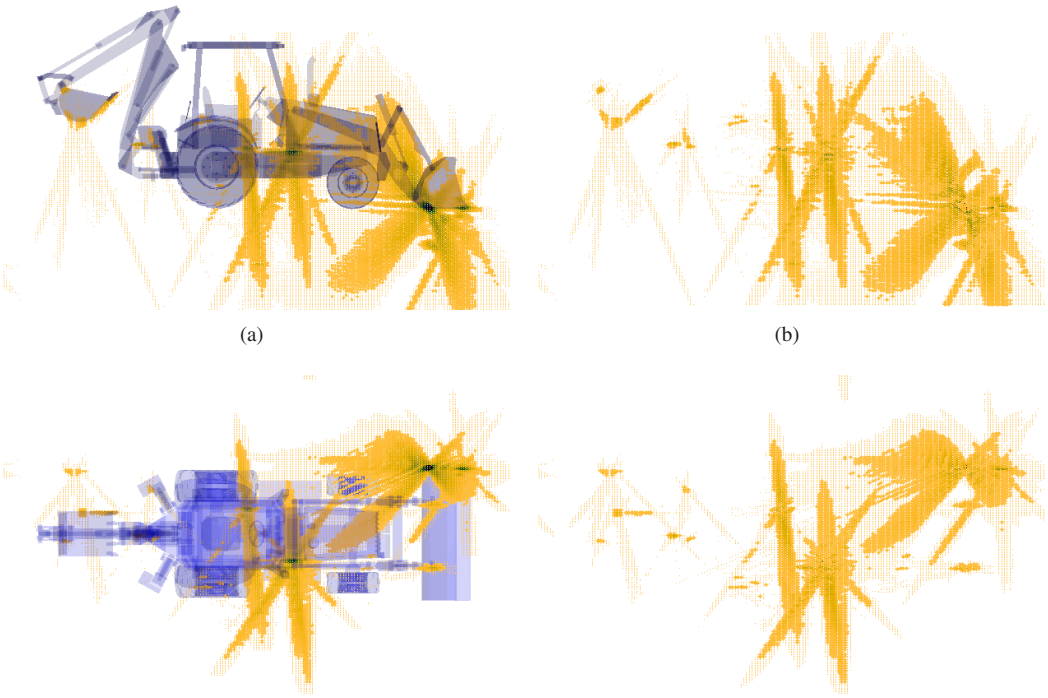

(a) (b)

(c) (d)

Fig. 6. Reconstructed backhoe from standard Fourier image reconstruction on each subset images for an SNR of 10 dB. Lighter colors and smaller points are used for smaller magnitude voxels; darker colors and larger points are used for larger magnitude voxels. Subfigure (a) and (b) show a side view of the reconstructed image with and without the backhoe facet model superimposed, respectively; subfigures (c) and (d) show top views of the reconstructed image with and without the backhoe facet model superimposed, respectively. The top 25 dB magnitude image voxels are displayed.

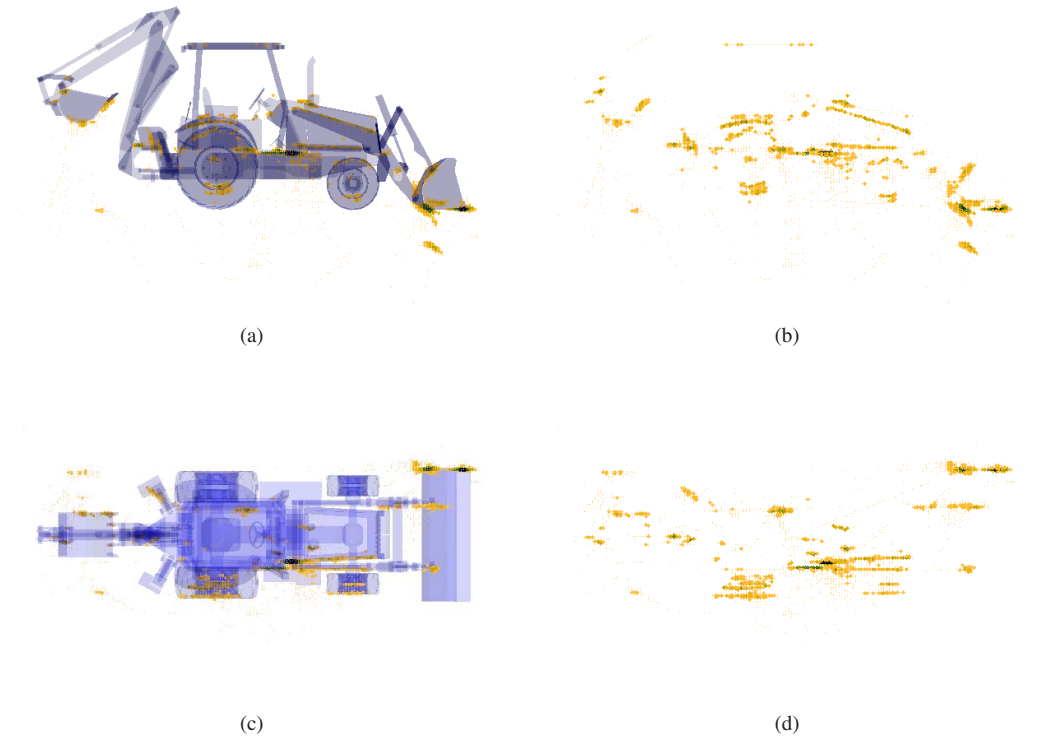

(a) (b)

(c) (d)

Fig. 7. Reconstructed backhoe image using Algorithm 1 for an SNR of 10 dB. Lighter colors and smaller points are used for smaller magnitude voxels; darker colors and larger points are used for larger magnitude voxels. Subfigure (a) and (b) show a side view of the reconstructed image with and without the backhoe facet model superimposed, respectively; subfigures (c) and (d) show top views of the reconstructed image with and without the backhoe facet model superimposed, respectively. The top 30 dB magnitude image voxels are displayed.

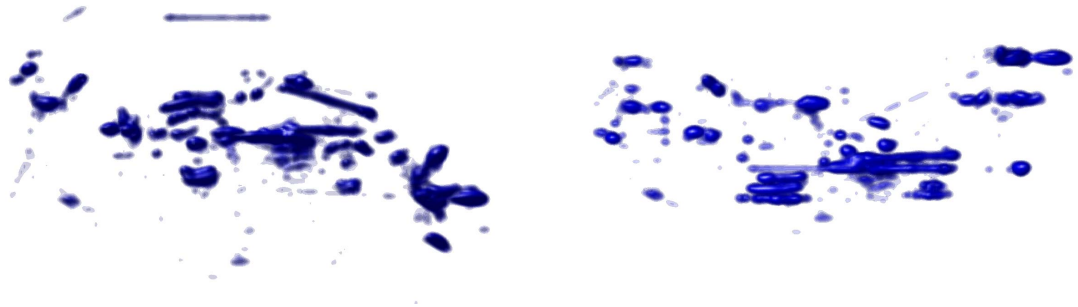

(a) (b)

Fig. 8. Post-processed reconstructed backhoe image using Algorithm 1 for an SNR of 10 dB. The image is represented as contours of smoothed voxel magnitudes. Color darkens and transparency becomes more opaque as contour level increases. Subfigure (a) shows a side view of the reconstructed image, and subfigure (b) shows a top view of the reconstructed image. The top 30 dB of magnitude contours are displayed.

V. Conclusion

In this paper, we presented a sparse imaging algorithm for reconstructing 3D SAR images from k-space data collected on an arbitrary flight path. The algorithm assumes that the number of scattering centers in a scene is sparse compared to the number of voxels in the reconstructed images and that scattering center response is approximately constant over narrow aspect angles. Images formed from subsets of k-space data at different polarizations and aspect angles are reconstructed and noncoherently combined to capture the response of non-persistent scattering and polarization-specific scattering in one image. An image reconstruction example using k-space data from a sparse continuous pseudorandom "squiggle" path was presented. This example demonstrated how standard Fourier imaging fails to produce accurate well resolved 3D images using a sparse collection of k-space data; it also demonstrated how sparse reconstruction can produce accurate, mostly artifact-free, well-resolved 3D SAR images from sparse, nonlinear flight paths.

Acknowledgment

The authors would like to thank Dr. Lee C. Potter for his suggestions while revising this document.

References

[1] C. V. Jakowatz Jr., D. E. Wahl, P. H. Eichel, D. C. Ghiglia, and P. A. Thompson, *Spotlight-Mode Synthetic Aperture Radar: A Signal Processing Approach*. Boston: Kluwer Academic Publishers, 1996.

[2] S. DeGraaf, "3-D fully polarimetric wide-angle superresolution-based SAR imaging," in *Thirteenth Annual Adaptive Sensor Array Processing Workshop (ASAP 2005)*. Lexington, M.A.: MIT Lincoln Laboratory, June 7–8 2005.

[3] M. Stuff, M. Biancalana, G. Arnold, and J. Garbarino, "Imaging moving objects in 3D from single aperture synthetic aperture radar," in *Proc. IEEE 2004 Radar Conference*, April 26–29 2004, pp. 94–98.

[4] C. D. Austin and R. L. Moses, "Interferometric synthetic aperture radar detection and estimation based 3D image reconstruction," in *Algorithms for Synthetic Aperture Radar Imagery XIII*. Orlando, FL.: SPIE Defense and Security Symposium, April 17–21 2006.

[5] J. Tsao and B. Steinberg, "Reduction of sidelobe and speckle artifacts in microwave imaging: the CLEAN technique," *IEEE Trans. on Antennas and Propagation*, vol. 36, no. 4, pp. 543–556, April 1988.

[6] M. Çetin and W. Karl, "Feature-enhanced synthetic aperture radar image formation based on nonquadratic regularization," *IEEE Trans. on Image Processing*, vol. 10, no. 4, pp. 623–631, April 2001.

[7] T. Kragh and A. Kharbouch, "Monotonic iterative algorithms for SAR image restoration," in *IEEE 2006 Int. Conf. on Image Processing*, Oct. 2006, pp. 645–648.

[8] R. Moses, L. Potter, and M. Çetin, "Wide angle SAR imaging," in *Algorithms for Synthetic Aperture Radar Imagery XI*. Orlando, FL.: SPIE Defense and Security Symposium, April 12–16 2004.

[9] K. Naidu and L. Lin, "Data dome: full k-space sampling data for high-frequency radar research," in *Algorithms for Synthetic Aperture Radar Imagery XI*. Orlando, FL.: SPIE Defense and Security Symposium, April 12–16 2004.

[10] S. Chen, D. Donoho, and M. Saunders, "Atomic decomposition by basis pursuit," *SIAM Journal on Scientific Computing*, vol. 20, no. 1, pp. 33–61, 1998.

[11] M. Figueiredo, R. Nowak, and S. Wright, "Gradient projection for sparse reconstruction: Application to compressed sensing and other inverse problems," *IEEE Journal of Selected Topics in Signal Processing*, vol. 1, no. 4, pp. 586–597, Dec. 2007.

[12] T. Hastie, R. Tibshirani, and J. Friedman, *The Elements of Statistical Learning*. Canada: Springer, 2001.

[13] R. Moses and L. Potter, "Noncoherent 2D and 3D SAR reconstruction from wide-angle measurements," in *Thirteenth Annual Adaptive Sensor Array Processing Workshop (ASAP 2005)*. Lexington, M.A.: MIT Lincoln Laboratory, June 7–8 2005.

[14] E. Ertin, L. Potter, and R. Moses, "Enhanced imaging over complete circular apertures," in *Fortieth Asilomar Conf. on Signals, Systems and Computers (ACSSC 06)*, Oct 29 – Nov. 1 2006, pp. 1580–1584.

[15] Air Force Research Laboratory. (2008, June) Backhoe data sample and Visual-D challenge problem. [Online]. Available: https://www.sdms.afrl.af.mil/main.php

[16] D. Malioutov, M. Çetin, and A. Willsky, "Homotopy continuation for sparse signal representation," in *Proc. IEEE Int. Conf. on Acoustics, Speech, and Signal Processing (ICASSP 05)*, vol. 5, March 2005, pp. 733–736.

[17] Ö. Batu and M. Çetin, "Hyper-parameter selection in non-quadratic regularization-based radar image formation," in *Algorithms for Synthetic Aperture Radar Imagery XV*. Orlando, FL.: SPIE Defense and Security Symposium, March 17–20 2008.